Journal of Materials Chemistry A

ROYAL SOCIETY OF CHEMISTRY

PAPER

View Article Online
View Journal | View Issue

Cite this: J. Mater. Chem. A, 2023, 11, 20724

Radiation-grafted anion-exchange membranes for CO_2 electroreduction cells: an unexpected effect of using a lower excess of *N*-methylpiperidine in their fabrication†

Terry R. Willson,[a] Carlos A. Giron Rodriguez,[b] Qiucheng Xu,[b] Jordan Frow,[c] Fabrizia Foglia,[d] Keenan Smith,[d] Ravikumar Ravikumar,[e] Mohanraj Vinothkannan,[e] Najet Mahmoudi,[f] Ihtasham Salam,[a] Arun Prakash Periasamy,[a] Daniel K. Whelligan,[a] Mohamed Mamlouk,[e] Hungyen Lin,[c] Brian Seger[b] and John R. Varcoe*[a]

Giron Rodriguez *et al.* [*ACS Sustainable Chem. Eng.*, 2023, **11**, 1508] previously showed that radiation-grafted anion-exchange membranes containing *N*-benzyl-*N*-methylpiperidinium headgroups (MPIP-RG-AEM) are promising for use in CO_2 electrolysis (*cf.* commercial and other RG-AEM types). For a more sustainable synthesis, MPIP-RG-AEMs have now been fabricated using a reduced 1.1 times excess of amine reagent (historically made using >5 times excess). A resulting RG-AEM promisingly had a bulk amination level that was comparable to those made with the traditional large excess. Unexpectedly, however, it had a significantly reduced water content, with two further batches showing that this observation was repeatable (and reproducible *via* measurements collected on a single batch using different techniques in different labs). The ionic conductivities of the RG-AEM made with a controlled 1.1 excess of amine were also lower, with higher activation energies. Terahertz time-domain spectroscopy measurements showed that the lower water uptake RG-AEMs, made with the 1.1 amine excess, contained smaller amounts of bulk water relative to bound water (a repeatable observation with different counter-anions). This lack of bulk water, yielding reduced water diffusion coefficients, led to a change in the water management when such RG-AEMs were tested in CO_2 electrolysis cells, with significantly affected *in situ* performances. Small angle scattering data (X-ray and neutron) indicated that MPIP-RG-AEM fabrication with the 1.1 excess of amine reduced the size of the amorphous lamella domains on hydration, and this change is suspected to be the cause of the lower water uptakes and swelling. The finding that chemically similar AEMs can have significantly different hydration properties is potentially important to all ion-exchange membrane users and developers (beyond the CO_2 electrolysis scope of this study).

Received 16th August 2023
Accepted 7th September 2023

DOI: 10.1039/d3ta04915a

rsc.li/materials-a

Background and aims of the study

A range of anion-exchange membranes (AEM) are being developed for evaluation in electrochemical cells that reduce CO_2 into high value chemicals and fuels (CO_2RR cells).[1–5] A class of high conductivity AEMs, that are stable to alkali at temperatures of 60 °C or above (depending on the hydration levels), can be made using the radiation-grafting method (RG-AEM, see Scheme 1 for the example discussed *vide infra*).[6–8] RG-AEMs have been developed in the EU project SELECTCO2 for evaluation in CO_2RR cells for the selective electroreduction of CO_2 to CO, ethanol, and ethylene.[9] To date, it has been found that RG-AEMs made from precursor 25 μm ETFE polymer films that contain the *N*-benzyl-*N*-methylpiperidinium (MPIP) quaternary ammonium (QA) chemistry have a higher *in situ* CO_2RR to CO performance compared to analogues containing both the *N*-benzyl-*N*-methylpyrrolidinium (MPY) and

[a]School of Chemistry and Chemical Engineering, The University of Surrey, Guildford GU2 7XH, UK. E-mail: j.varcoe@surrey.ac.uk
[b]Department of Physics, The Technical University of Denmark, Fysikvej, 312, DK-2800 Kgs. Lyngby, Denmark
[c]School of Engineering, Lancaster University, Lancaster LA1 4YW, UK
[d]Department of Chemistry, Christopher Ingold Laboratory, University College London, London WC1H 0AJ, UK
[e]School of Engineering, Merz Court, Newcastle University, NE1 7RU, UK
[f]ISIS Neutron and Muon Source, Science & Technology Facilities Council, Rutherford Appleton Laboratory, Harwell Science and Innovation Campus, Chilton OX11 0QX, UK

† Electronic supplementary information (ESI) available. See DOI: https://doi.org/10.1039/d3ta04915a. Raw data is also available at DOI: https://doi.org/10.6084/m9.figshare.22353862 (CC-BY).

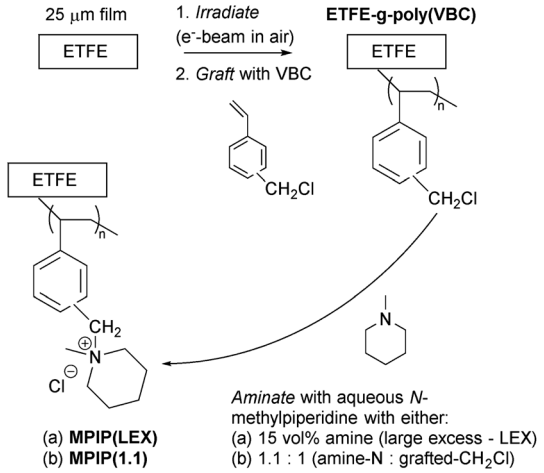

Scheme 1 A summary of the synthesis process used to fabricate the two MPIP-based RG-AEMs: (a) MPIP(LEX) fabricated using a large (>5×) excess of *N*-methylpiperidine; and (b) MPIP(1.1) fabricated using a 1.1 : 1 controlled excess of *N*-methylpiperidine. The RG-AEMs were fabricated in the Cl^- forms but can be converted to other anion forms *via* submersion in aqueous anion solutions.

benzyltrimethylammonium (TMA) QA-chemistries (the latter more tailored for use in hydrogen technologies).[10]

In 2017, the method for producing RG-AEMs was improved by replacing the organic solvent (propanol) in the grafting mixture with water.[11] This switch to an aqueous grafting formulation greened the process and allowed for lower concentrations of vinylbenzyl chloride (VBC) monomer to be used (and re-used). This radiation grafting process introduces electrophilic benzyl chloride groups into the resulting ETFE-*g*-poly(VBC) membranes (Scheme 1), which can then be reacted with nucleophilic tertiary amines to form the desired cationic QA-groups and create anion-conducting RG-AEMs.[7] Because of the insoluble nature of the grafted ETFE-*g*-poly(VBC) membranes, this post-grafting amination step traditionally used a large excess of tertiary amines such as *N*-methylpiperidine.

With a further reduction in chemical waste in mind, we have now investigated if a lower (more stoichiometric) excess of amine could be used (*e.g.* 1.1 : 1 mol% of tertiary amine N : –CH_2Cl groups). The null hypothesis was that this smaller excess of amine would lead to identical RG-AEMs. We show that this smaller excess of *N*-methylpiperidine can be used to produce an MPIP-type RG-AEM that is chemically comparable to that made using a larger excess of amine (see the ESI Section A† for select complimentary data on ETFE-MPY and HDPE-MPIP analogues). However, we also show that, unexpectedly, the use of a lower excess of *N*-methylpiperidine leads to RG-AEMs with lower *ex situ* water contents and anion conductivities, and poorer CO_2RR cell performances at higher current densities.

Materials and methods

Chemicals and materials

Nowoflon ET-6235Z ethylene-tetrafluoroethylene (ETFE) polymer film (25 μm thick) was supplied by Nowofol Kunststoffprodukte GmbH (Germany). Vinylbenzyl chloride (VBC, also known as chloromethylstyrene, *ca.* 96% purity, 43 mol% *para*- and 57 mol% *meta*-isomer mix, containing 50–100 ppm *tert*-4-butylcatechol and 700–900 ppm nitroparaffin inhibitors) was purchased from Polysciences GmbH and used as supplied without any inhibitor removal prior to use in the grafting mixtures. 1-Octyl-2-pyrrolidone dispersant and *N*-methylpiperidine (99%) were purchased from Sigma-Aldrich (Merck) and used as supplied. Acetone was of reagent grade. Aqueous $AgNO_3$ titration standard solutions were purchased from Honeywell or Fluka and used as supplied. The ultra-pure water (UPW) used throughout this study was generated using a Purite water purification system (resistivity = 18.2 MΩ cm).

Synthesis of ETFE-*g*-poly(VBC) intermediate membranes

A summary of the synthesis of the MPIP-based RG-AEMs is presented in Scheme 1. The grafting of the commercial 25 μm thick ETFE film used the previously reported pre-irradiation in air (peroxidation) method.[11] The variable being investigated in this study was the level of excess of *N*-methylpiperidine used to aminate the ETFE-*g*-poly(VBC) grafted membranes.

For the irradiation step, ETFE films were subject to electron-beam irradiation in air (at room temperature) to a total absorbed dose of 40 kGy using a continuous vertical 10 MeV Electron Beam Accelerator (Synergy Health Sterilisation UK Limited, Daventry facility, UK). The irradiated films were immediately stored under solid CO_2 (−79 °C) for transport back to the University of Surrey where they are transferred to a −40 °C freezer for storage before being used for grafting.

For the grafting step, e^--beamed ETFE films (*ca.* 12 × 12 cm each) were submerged in an aqueous grafting mixture containing excess VBC (5 vol%) and 1-octyl-2-pyrrolidone (1 vol%). The grafting solution was then purged with N_2 for 1 h before the vessel was sealed and heated to 70 °C for 24 h. Post-grafting, the ETFE-*g*-poly(VBC) membranes were thoroughly washed in acetone to remove any residual VBC or non-grafted poly(VBC) homopolymer. The washed ETFE-*g*-poly(VBC) grafted membranes were then dried at 50 °C under vacuum for 3 h.

The degree of grafting (DoG, %) of each fabricated ETFE-*g*-poly(VBC) batch was calculated using:

$$\mathrm{DoG}(\%) = 100 \times \left(\frac{m_g - m_i}{m_i}\right) \quad (1)$$

where m_g is the mass of the grafted membranes and m_i is the mass of the irradiated films (before grafting). The amount (mol) of grafted –CH_2Cl groups in a ETFE-*g*-poly(VBC) membrane could be calculated using:

$$n(-\mathrm{CH_2Cl}) = \frac{m_g - \left(m_g \times 100/(100 + \mathrm{DoG})\right)}{\mathrm{MW_{VBC}}} \quad (2)$$

where m_g is the mass of the grafted membrane and $\mathrm{MW_{VBC}}$ is the molecular weight of the repeat units of the poly(VBC) grafted chains (152.62 g mol^{-1}).

Amination of ETFE-*g*-poly(VBC) membranes to form RG-AEMs

After characterisation, each ETFE-*g*-poly(VBC) membrane batch was cut in half. Each half was then aminated using two different amination methods:

(1) One half was submerged in an aqueous *N*-methylpiperidine (15 vol%, large >5 times excess) solution in a sealed vessel at 60 °C for 18 h to form the RG-AEM designated MPIP(LEX).

(2) The second half was submerged in an aqueous *N*-methylpiperidine solution (containing 1.1 mol tertiary amine N atoms for every 1 mol of $-CH_2Cl$ groups in the grafted membrane) at 60 °C for 18 h to form the RG-AEM designated MPIP(1.1).

After amination, all RG-AEMs were thoroughly washed in UPW and heated in fresh UPW at 70 °C for 18 h. This was to ensure that all excess, unreacted *N*-methylpiperidine was removed.

To ensure the pure Cl^- anion forms, the as synthesised RG-AEMs were submerged in aqueous NaCl solution (1 mol dm^{-3}) for 1 h with the NaCl solution being refreshed three times during this ion-exchange period. They were then removed and thoroughly washed in UPW to remove any excess co-ions (Na^+) and counter-ions (Cl^-), such that the only Cl^- present were charge balancing the positively charged QA groups. The final pristine Cl^- form RG-AEM samples were then stored under UPW, in a fully hydrated state, until required for further characterisation or experiments.

Raman spectro-microscopy

Raman spectra were recorded with dry samples of the ETFE-*g*-poly(VBC) membrane (prior to amination) and each Cl^- form RG-AEM (after amination with each method). Raman spectra were recorded on $n = 100$ random locations across both surfaces of the ETFE-*g*-poly(VBC) membrane and on $n = 50$ random locations across both surfaces of each RG-AEM using a Renishaw InVia Reflex Raman Microscope equipped with a 785 nm excitation line laser (300 mW) and a 20× (NA = 0.40) objective. These surface spectra were used to confirm homogenous graft distribution and amination. Cross-sectional Raman line-maps were collected across the core of each RG-AEM (1.5 μm steps) using the same instrument but with a 50× objective (NA = 0.50, with pin-hole, calculated Airy minimum laser spot diameter 2 μm), 5 s exposure time and 16 accumulations per spectra. Cross-sectional line-mapping was used to evaluate the through-core reaction of $-CH_2Cl$ groups with *N*-methylpiperidine with both amination methods. All Raman data was collected and baselined corrected using Renishaw WiRE Software (Renishaw PLC, UK) with further processing (peak height normalisation) and data analysis (peak area integration) carried out using Spectragryph Optical Spectroscopy Software (Spectroscopy Ninja, Germany).

Solid-state NMR

Solid-state NMR spectra were recorded with dry samples of the ETFE-*g*-poly(VBC) membrane and each Cl^- form RG-AEM (after amination with each method). The instrument used was a Bruker Avance III HD spectrometer and samples were loaded into a 3.2 mm (rotor outer diameter) magic-angle spinning (MAS) probe (except for ^{15}N measurements where a 4 mm rotor was used). The acquisition conditions were established from a series of short optimisation measurements.

Carbon-13 spectra were recorded at 100.63 MHz (for C). The spectra were obtained using cross-polarisation at a sample spin-rate of 12 kHz with a 1 s recycle delay and 1 ms contact time. Dual ^{19}F and ^1H decoupling was applied. Spectral referencing was with respect to an external sample of neat tetramethylsilane (carried out by setting the high-frequency signal from adamantane to 38.5 ppm).

Fluorine-19 spectra were recorded at 376.51 MHz (for F). Spectra were obtained using direct excitation at a spin-rate of 20 kHz and with a recycle delay of 4 s. ^1H decoupling was applied. Spectral referencing is with respect to $CFCl_3$ (carried out by setting the signal from an external sample of 50% CF_3COOH in H_2O to −76.54 ppm). Spinning sidebands were identified by re-recording a spectrum of ETFE at a spin rate of 22 kHz and looking for peak shifts (*cf.* spectrum at 20 kHz).

Nitrogen-15 spectra were recorded at 40.55 MHz (for N). The spectra were obtained using cross-polarisation at a sample spin-rate of 12 kHz with a 4 s recycle delay and 10 ms contact time. ^1H decoupling was applied. Spectral referencing was with respect to an external sample of nitromethane (carried out by setting the high-frequency signal from glycine to 346.8 ppm).

Thermogravimetric analysis (TGA)

Thermogravimetric analysis (TGA) was performed on a TA Instruments TGA Q500 with sample mass of *ca.* 5 mg (Cl^- forms) placed into a Pt crucible. Heating was from ambient temperature to 600 °C at 10 °C min^{-1} under flowing N_2.

Gravimetric water uptake (WU) and swelling

After a Cl^- form RG-AEM sample was removed from UPW storage, the excess surface water was quickly removed by dabbing the sample with filter paper. The mass (m_h, analytical balance to ± 0.2 mg), thickness (t_h, micrometer to ± 2 μm), and area (A_h, steel ruler to ± 0.5 mm) of the hydrated sample were then immediately recorded (before too much water had evaporated from the sample). After drying of the sample under vacuum at 50 °C for at least 18 h, the mass (m_d), thickness (t_d), and area (A_d) were quickly re-recorded (before adsorption of atmospheric water). The gravimetric water uptake (WU), through-plane swelling (TPS), and area swelling (AS) of each Cl^- form RG-AEM sample were calculated as follows:

$$\mathrm{WU}(\%) = 100 \times \frac{m_h - m_d}{m_d} \quad (3)$$

$$\mathrm{TPS}(\%) = 100 \times \frac{t_h - t_d}{t_d} \quad (4)$$

$$\mathrm{AS}(\%) = 100 \times \frac{A_h - A_d}{A_d} \quad (5)$$

All measurements were repeated on $n = 3$ samples of each RG-AEM. The number of H_2O molecules per QA group on the RG-AEM samples, $\lambda(H_2O)$, were calculated using:

$$\lambda(H_2O) = \frac{\mathrm{WU}(\%)/100}{\mathrm{IEC} \times M_{\mathrm{water}}} \quad (6)$$

where the ion-exchange capacity (IEC) was determined as described below and M_{water} is the molar mass of water.[6]

Ion-exchange capacity (IEC)

A sample of Cl^- form RG-AEM that had been vacuum dried at 50 °C for at least 18 h (dried mass m_d) was immersed in 25 cm^3 of aqueous $NaNO_3$ solution (1.2 mol dm^{-3}) and continuously stirred for 16 h. The solution (still containing the RG-AEM sample) was subsequently acidified with aqueous 1 cm^3 HNO_3 (2 mol dm^{-3}) and titrated against aqueous $AgNO_3$ analytical standardised solutions (C = 0.02000 ± 0.00006 mol dm^{-3}). A Metrohm 848 Titrino Plus autotitrator equipped with an Ag-Titrode (Cl^- anion selective electrode) was used for the titrations (operating with dynamic end point mode). The end point (V_{EP}) was taken at the peak in the dE/dV plot of potential (E) *vs.* volume (V), *i.e.* the maximum gradient in the E *vs.* V curve. The IEC (mmol g^{-1}) for each sample was calculated using:

$$\mathrm{IEC} = \frac{V_{EP} \times C}{m_d} \quad (7)$$

Repeat IEC measurements were recorded on n = 3 samples of each RG-AEM.

Repeat fabrication of ETFE-*g*-poly(VBC) batches

The initial results presented in this paper (with extensive spectroscopic characterisation) were from a batch of ETFE-*g*-poly(VBC) intermediate membrane with a DoG = 73%, that was then aminated using both methods MPIP(LEX) and MPIP(1.1) (to give IECs of 1.8 and 1.7 mmol g^{-1}, respectively – see Table 1). Due to this initial batch being used up in these experiments, two further batches of ETFE-*g*-poly(VBC) were fabricated (DoG = 67 and 81%) that were both aminated using both methods (designated MPIP(LEX)-Bx and MPIP(1.1)-Bx, where x = 2 for batch 2 and x = 3 for batch 3). These new batches were used for to check repeatability and to allow further experiments

Table 1 Key *ex situ* properties[11] of the Cl^--form RG-AEMs made from ETFE-*g*-poly(VBC) grafted intermediates with stated degrees of grafting (DoG) [three batches]. Errors are sample standard deviations from measurements on n = 3 samples of each RG-AEM

	MPIP(LEX)	MPIP(1.1)	MPIP(LEX)-B2	MPIP(1.1)-B2	MPIP(LEX)-B3	MPIP(1.1)-B3
Batch	1		2		3	
DoG of grafted precursor (%)	73		67		81	
IEC/mmol g^{-1}	1.80 ± 0.01	1.71 ± 0.03	1.70 ± 0.10	1.60 ± 0.02	1.85 ± 0.06	1.80 ± 0.06
Thickness (dry)/μm	47 ± 2[a]	50 ± 2[a]	46 ± 2[a]	48 ± 2[a]	52 ± 2[a]	48 ± 2[a]
Thickness (hydrated)/μm	62 ± 2[a]	59 ± 2[a]	64 ± 2[a]	56 ± 2[a]	61 ± 2[a]	53 ± 2[a]
TPS (%)	32 ± 6[b]	18 ± 6[b]	39 ± 6[b]	16 ± 6[b]	17 ± 5[b]	10 ± 6[b]
AS (%)	38 ± 3	24 ± 3	52 ± 4	29 ± 5	77 ± 2	36 ± 2
WU (%)	77 ± 1	33 ± 3	95 ± 2	31 ± 2	94 ± 2	42 ± 1
$\lambda(H_2O)$	23 ± 1[b]	11 ± 1[b]	31 ± 2[b]	11 ± 1[b]	28 ± 1[b]	13 ± 1[b]

[a] Errors are sample standard deviations from n = 3 measurements on each membrane or 2 μm (the minimum visual precision of the micrometer used), whichever is the greatest. [b] Errors are propagated uncertainties (calculated from the errors of input parameters).

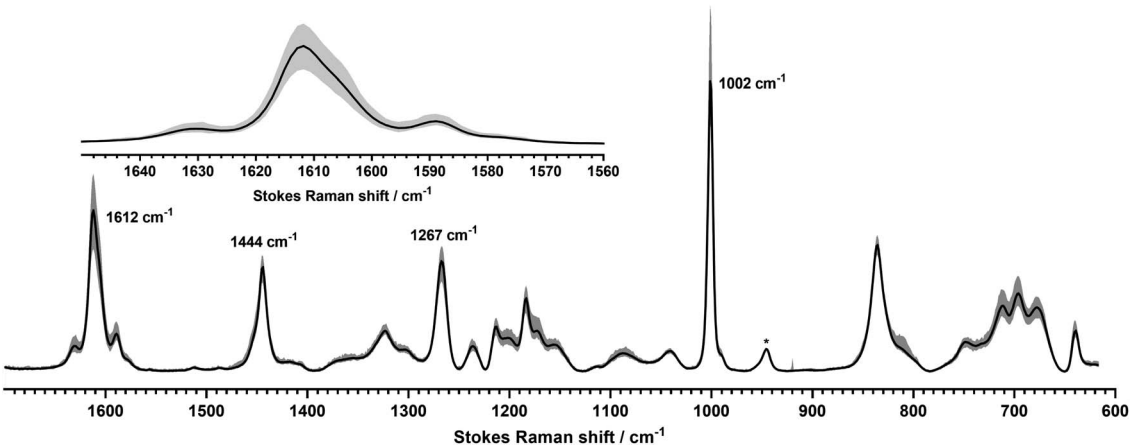

Fig. 1 Raman data (λ = 785 nm line laser, 20× NA = 0.40 objective) collected on the ETFE-*g*-poly(VBC) intermediate membrane (DoG = 73%) used to produce the MPIP(LEX) and MPIP(1.1) in this study. This data is derived from n = 100 individual spectra recorded at random locations across both surfaces of the membrane. The black line represents the averaged (mean) spectra. The grey envelope shows the range of intensities recorded at each Raman shift (minimum to maximum values obtained). *Spectral intensities were normalised to the ETFE-derived band at 945 cm^{-1} to aid visual comparison. The inset presents more detail around the 1612 cm^{-1} band from the poly(VBC) grafted chains. Cosmic rays were not removed (see grey peak at 920 cm^{-1}).

including CO_2RR cell tests and the more detailed characterisation described below.

Ion-exchange to the HCO_3^- or CO_3^{2-} RG-AEM forms

For some experiments discussed below, the RG-AEMs were required in the predominant OH^-, HCO_3^- and CO_3^{2-} forms (note, that due to unavoidable aqueous $HCO_3^- \rightleftharpoons CO_3^{2-} \rightleftharpoons OH^-$ equilibria, (bi)carbonate forms of AEMs are still alkaline and contain OH^- anions). To achieve this, the RG-AEM samples were submerged in either aqueous NaOH (purged of CO_2 and handled in a CO_2-free environment), $NaHCO_3$, or Na_2CO_3 (all 1 mol dm^{-3}) for 1 h with the solution being refreshed three times during this ion-exchange period. The samples were then thoroughly washed in UPW to remove any excess co-ions and counter-ions. Colour guide to Fig. 1–14 related to the predominant anion forms present: Cl^- = black, CO_3^{2-} = red, HCO_3^- = blue, OH^- = teal.

In-plane (4 probe) anion conductivities in water (fully hydrated)

The anion conductivities of fully hydrated MPIP(LEX)-B3 and MPIP(1.1)-B3 samples were measured using a Solartron 1260/1287 combination controlled by ZPlot/ZView software (Scribner Associates, USA). Impedance spectra were collected over a frequency range of 1 Hz–100 kHz (10 mV amplitude). Samples were mounted in a 4-probe BekkTech BT-112 test cell (Alvatek, UK) and submerged in UPW at controlled temperatures. Ionic resistance values taken as the low frequency x-axis intercept in the collected Nyquist plots, which were then used to calculate the conductivity (σ/mS cm^{-1}) using:

$$\sigma = \frac{l}{Rwt} \tag{8}$$

where l is the distance between the Pt sense electrodes (0.425 cm), and w and t are the width and thickness of the RG-AEM sample under test, respectively. Repeat conductivity measurements were recorded on $n = 3$ samples of MPIP(LEX)-B3 and MPIP(1.1)-B3 in each anion form tested.

Terahertz time-domain spectroscopy (THz-TDS) investigation of the states of water

Molecular water states were resolved using the recently reported THz-TDS.[12] Samples of MPIP(LEX)-B3 and MPIP(1.1)-B3 (in Cl^-, HCO_3^- and CO_3^{2-} anion forms) were prepared into 4 cm × 4 cm size and hydrated at *ca.* 20 °C over 24 h in UPW. Measurements were taken using a THz-TDS system (TERA K15, Menlo Systems, Germany) operating between 0.1 and 3 THz on the hydrated samples at ambient conditions (20 °C, relative humidity (RH) = 45%) in the first 60 s to minimise dehydration. As a standard routine for all measurements, a reference measurement is always acquired without the sample being present and taken immediately before the sample measurement to remove potential baseline drift. The acquired waveform of the THz electric field for both sample and reference measurements are then converted to the frequency domain by fast Fourier transform, which is then analysed using custom-developed analysis algorithm for water states extraction.[12]

Dynamic water vapour sorption (DVS)

The water uptakes dynamics of MPIP(LEX)-B3 and MPIP(1.1)-B3 were measured as a function of RH at 25 °C using a dynamic water vapor sorption analyser (DVS, IGsorp from Hiden Isochema). For completeness, the OH^- forms were additionally studied; this was possible in this set-up as CO_2 could be adequately excluded during AEM handing and measurements, unlike the other experiments described in this article.

Each sample was first dried at RH = 0% at 60 °C for 1 h to achieve the dry state to estimate the dry weight (m_d). The sample was then hydrated at 25 °C with increasing RH using a humidified N_2 feeds (equilibrated for 1 h at each RH). The water uptake was calculated from the wet weight (m_{RH}) at each equilibrium step using eqn (3) (with m_{RH} replacing m_h). The water contents, $\lambda(H_2O)$, at each RH could then be calculated using eqn (6).

Kinetics of water uptake (transient sorption) was estimated using the measured weight change as a function of time at each RH step. The mass (m) increase over time was assumed to be diffusion limited and follows Fick's second law of diffusion:

$$\frac{m_t}{m_\infty} = 1 - e^{-k_s t} = 1 - e^{-t/\tau} \tag{9}$$

where m_t is the mass of water absorbed at time t, m_∞ is the mass of water absorbed at thermodynamic equilibrium, k_s is inverse time constant, and τ is the time constant. The water diffusion coefficient, D_w, was estimated from k_s (obtained from eqn (9)) and the film thickness, L, using:

$$D_w = k_s L^2 \tag{10}$$

CO_2RR cell testing

For the electrochemical CO_2RR testing of MPIP(LEX)-B3 and MPIP(1.1)-B3, commercial porous Ag membranes (Sterlitech, thickness of 50 μm, porous size of 1.2 μm) and commercial IrO_2-coated carbon papers (Dioxide Materials) were used as cathode gas diffusion electrodes (GDE) and anode GDEs, respectively. All the CO2RR testing were performed in a 2.25 cm^2 membrane electrode assembly (MEA)-based CO_2 electrolyser. Each MEA is assembled by placing the as-prepared RG-AEMs (in the HCO_3^- form) between a cathode GDE and an anode GDE. PFA gaskets were then put in place for sealing. A titanium serpentine flow field was used on the anode side, while a graphite serpentine flow field was used on the cathode side. The cell was assembled with a torque of 3 N m to guarantee sufficient compression and avoid leakages out of the system.

During the CO_2RR testing at room temperature, dry CO_2 gas was supplied to the cathode flow field with a flow rate of 30 cm^3 min^{-1} (293 K and 1 $bar_{absolute}$) using a mass flow controller (Vöegtlin red-y smart series), while the anode was fed with aqueous $KHCO_3$ (0.1 mol dm^{-3} concentration, made from $KHCO_3$ purchased from Sigma-Aldrich, 99.99% metal basis). A constant

volume of 40 cm^3 anolyte was recirculated through the anode with a diaphragm pump (KNF NF1.5TTDCB-4) at 40 cm^3 min^{-1}.

Electrochemical measurements were initially performed under galvanostatic mode with a potentiostat (Biologic SP-300) and the cell voltages are reported without any *iR* correction. Data was also collected under potentiostatic mode at cell voltages of 3.0 and 3.2 V *vs.* a Ag/AgCl (aqueous 3 mol dm^{-3} NaCl) reference electrode, which was placed at the anode flow plate to record the uncompensated resistances.

Gas products from CO_2RR were measured using a PerkinElmer Clarus 590 gas chromatograph equipped with Molecular Sieve 13×, and HayeSep Q pack column, coupled with flame ionization and thermal conductivity detectors.

Dynamic mechanical analysis (DMA)

DMA measurement were conducted using a TA Instruments DMA Q800 and a multi-Frequency strain module. The batch 3 RG-AEM samples were mounted in a tension clamp and subjected to a temperature ramp of 5 °C min^{-1} between −100 and 180 °C (in air). A sinusoidal strain of 0.1% was applied with a frequency = 1 Hz. Multiple ($n = 3$) samples of both MPIP(LEX)-B3 and MPIP(1.1)-B3 were analysed where the data for each RG-AEM is an average response (the storage and loss moduli values were averaged to the closest integer temperature value).

Small angle X-ray and neutron scattering (SAXS and SANS)

Sample films were equilibrated at RH = 0 and 100% (pad-dried of excess of surface water after batch 3 RG-AEM samples were previously immersed in liquid H_2O or D_2O) and sandwiched between either Kapton (50 μm; SAXS) or quartz (SANS) windows and hermetically sealed. Scattering patterns were radially averaged to obtain intensity profiles ($I(Q)$), where scattering vector, Q, is defined by:

$$Q = \frac{4\pi}{\lambda}\sin\left(\frac{\theta}{2}\right) \quad (11)$$

with λ and θ being the wavelength and scattering angle, respectively.

SAXS profiles were recorded on a Ganesha 300XL, Xenocs, France. Microfocus X-ray ($\lambda = 1.54$ Å) was generated from a Cu source with a motorised collimation system of 4-blade single crystal slits. A movable solid-state photon-counting detector (PILATUS 300 K, Dectris AG, Switzerland) was mounted on an uninhibited transverse rail along the beamline. The SAXS system was calibrated using lanthanum hexaboride and validated on the day of measurement with silver behenate. SAXS profiles ($0.0035 \leq Q \leq 0.3$ $Å^{-1}$) were acquired with 1800 s exposure times under $<10^{-2}$ mbar vacuum.

SANS measurements were performed on the ZOOM beamline at the ISIS pulsed neutron source (Target Station 2, STFC Rutherford-Appleton Laboratory, UK), which employs neutrons separated by time-of-flight. Profiles were acquired using neutrons of wavelengths 1.75–14.4 Å, which are recorded on a 15 × 1 m^2 2D-detector placed at 4 m from the sample, which gives a scattering vector in the range $0.0045 \leq Q \leq 0.8$ $Å^{-1}$. SANS raw data were processed using the Mantid framework[13] and placed on an absolute scale (cm^{-1}) using the scattering from a standard sample (a solid blend of hydrogenous and perdeuterated polystyrene) in accordance with established procedures.[14]

Results and discussion

Raman spectral characterisation of the ETFE-*g*-poly(VBC)

Before amination, the surfaces of the ETFE-*g*-poly(VBC) (DoG = 73%) membrane were characterised using Raman (Fig. 1). The largest intensity variations across the 100 spectra recorded are located around the Raman bands that derive from the grafted

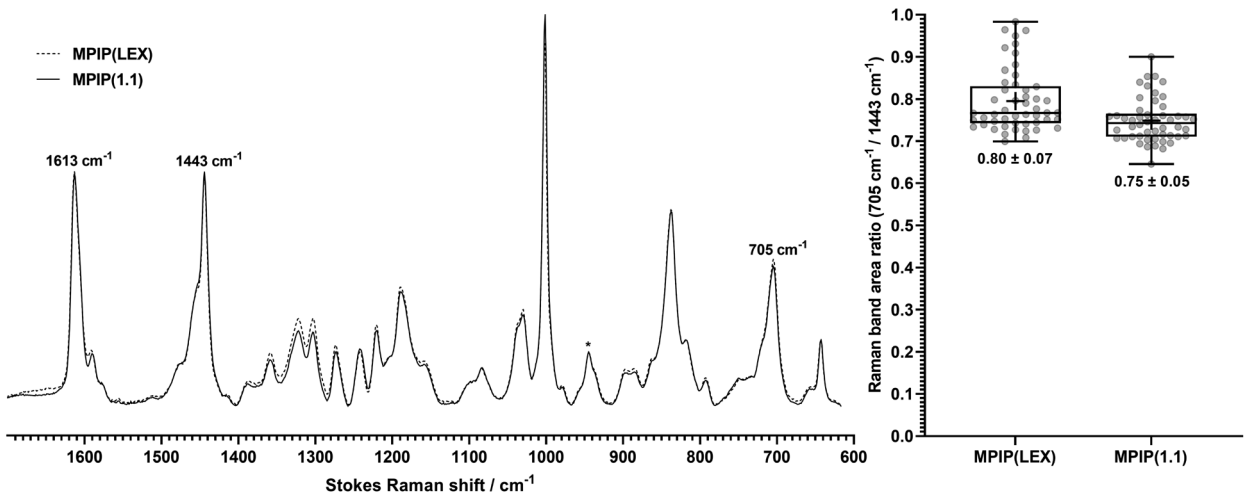

Fig. 2 (Left) Raman spectra ($\lambda = 785$ nm line laser, 20× NA = 0.40 objective) of MPIP(LEX) (dashed) and MPIP(1.1) (solid) where each spectra presented is the average of 50 spectra recorded at random locations on both sides of each RG-AEMs. *Spectral intensities were normalised to the ETFE-derived band at 945 cm^{-1} to aid visual comparison. (Right) Box plot of the calculated band area ratios (integrated area of the 705 cm^{-1} MPIP-derived band normalised to the integrated area of the 1443 cm^{-1} ETFE-derived band) for all 50 spectra recorded on each RG-AEM: whiskers = min and max, box = interquartile range, middle line = median, + = mean, grey dots = individual values for band area ratios, and the values below each box = mean ± sample standard deviation.

poly(VBC) chains (*e.g.* 1612, 1267 1002, and 695 cm^{-1})[7,15,16] with ETFE-derived bands showing less variations in intensities (*e.g.* 1444 and 836 cm^{-1}) as expected. This shows that there is some inhomogeneity in the grafting levels across the ETFE-*g*-poly(VBC) membrane. To quantify the level and significance of this inhomogeneity, the integration of the area of the 1612 cm^{-1} band (aromatic ring quadrant mode in the poly(VBC) grafted chains) normalised to the area of the ETFE-derived 1444 cm^{-1} band (ETFE CH_2 scissor mode band) yields a mean band area ratio of 1.89 with a sample standard deviation of 0.08 ($n = 100$). This corresponds to a relative standard deviation (RSD) of 4%, which can be taken as a quasi-measure of only a low level of grafting inhomogeneity.[17]

Raman spectral characterisation of MPIP(LEX) and MPIP(1.1)

The averaged Raman spectra for the surfaces of both MPIP(LEX) and MPIP(1.1) are presented in Fig. 2 (left), where each spectrum is the mean of $n = 50$ spectra recorded at random points both surfaces of each RG-AEM. These spectra confirm successful amination of the surfaces for both RG-AEMs where the band at 1268 cm^{-1} (due to the $-CH_2Cl$ groups in the grafted poly(VBC) chains) is not detectible and new bands at 705 and 1274 cm^{-1} have appeared that are highly diagnostic of MPIP groups.[7,15,16] This qualitative data representation shows a small reduction in the surface amination level of MPIP(1.1) compared to MPIP(LEX) (lower average bend intensity at 705 cm^{-1}).

For a more quantitative analysis of variations in surface amination, both intra-RG-AEM and between MPIP(LEX) and MPIP(1.1), the band area ratios (integrated area of the MPIP-derived 705 cm^{-1} band normalised to the integrated area of the 1443 cm^{-1} band that is predominantly due to the ETFE constituent) were calculated for all spectra and presented as box plots (Fig. 2 right). The RSD ($n = 50$) for MPIP(LEX) was 9% and for MPIP(1.1) was 7%. These variances were statistically different (*F*-test at 95% confidence level with $p = 0.0153$). MPIP(1.1) had a 6% lower mean level of surface amination than MPIP(LEX) (mean band area ratio of 0.75 *vs.* 0.80) and a 4% lower median (0.74 *vs.* 0.77). Both sets of data failed normality tests (*e.g.* $p = 0.0072$ for MPIP(LEX) and $p = 0.0337$ for MPIP(1.1) with the D'Agostino & Pearson test) so the Mann–Whitney test was applied to compare the two Raman band area ratio datasets. This test suggested the datasets were statistically different at the 95% confidence level (exact two-tailed $p = 0.0004$). The Kolmogorov–Smirnov test also indicated a statistical difference (approximate $p = 0.0120$).

For additional confidence, the Raman surface data was also quickly analysed where the area of the 705 cm^{-1} bands were normalised to the area of the smaller ETFE-derived bands at 945 cm^{-1}. This gave band area ratios of 3.0 ± 0.3 ($n = 50$, RSD = 10%) for MPIP(LEX) and 2.8 ± 0.3 ($n = 50$, RSD = 11%) for MPIP(1.1). This corresponds to 7% lower mean band area ratio for the latter, which is consistent with the above.

When changing the amination procedure, it is also important to assess if amination occurs homogeneously through the bulk (core) of the resulting RG-AEMs and not just laterally on the surface. Raman analyses was therefore conducted by recording 3 spatially separated line-maps through the core of a sample of each RG-AEM, where each line-map involved recording spectra in 1.5 μm steps from one surface to the other and calculating the band area ratios (integrated area of the 705 cm^{-1} band normalised to the integrated area of the 1443 cm^{-1} band). As can be seen in Fig. 3 (left-hand plot), the distributions of MPIP groups in both MPIP(LEX) and MPIP(1.1) are noisy but generally overlapping (similar amination levels) with no dip that would indicate lower amination levels in the cores of the RG-AEMs. Note for both RG-AEMs, the thicknesses appear smaller compared to the dry thicknesses presented in Table 1 as the cross-sectioned membranes are under

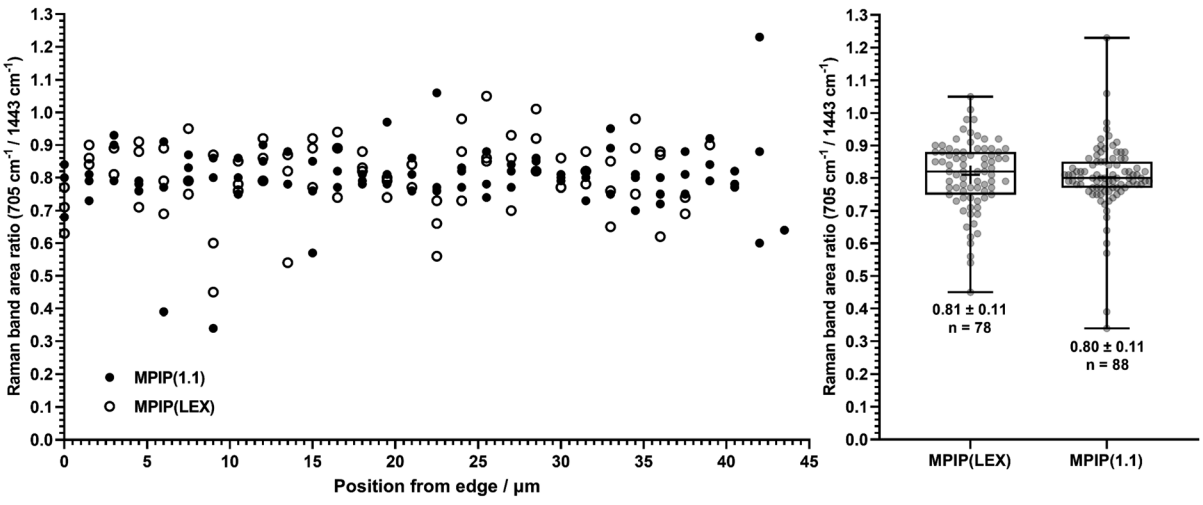

Fig. 3 (Left) Raman line-map data ($\lambda = 785$ nm, 50× NA = 0.50 objective) of MPIP(LEX) (dashed) and MPIP(1.1) (solid) where each spectra in each line-map (three per RG-AEM) were recorded in 1.5 μm steps from one surface to the other (band area ratio data calculated form the integrated area of the 705 cm^{-1} MPIP-derived band normalised to the integrated area of the 1443 cm^{-1} ETFE-derived band). (Right) Box plot of band area ratios (data from the 3 line-maps for each RG-AEM were combined): whiskers = min and max, box = interquartile range, middle line = median, + = mean, grey dots = individual values for band area ratios, and the values below each box = mean ± sample standard deviation.

compression in the sample holder (with potential shielding of the very edges of the RG-AEMs due to the metal holder).

For statistical analyses, the band area ratios for the 3 linemaps for each RG-AEM were combined and the data presented as box plots (Fig. 3 right). The RSDs across the band area ratios (amination distributions) was 14% for both MPIP(LEX) ($n = 78$) and MPIP(1.1) ($n = 80$). There was no significant difference between these variances (*F*-test at 95% confidence level with $p = 0.9960$). On first glance, the mean and median amination levels were the same within experimental precision (mean band area ratios were within 0.01 of each other and well within the sample standard deviations of 0.11, while the median band area rations were within 0.02 of each other). Both the MPIP(LEX) and MPIP(1.1) data failed the normality test ($p < 0.007$ with the D'Agostino & Pearson test) so the Mann–Whitney test was applied to compare the two Raman band area ratio datasets. This test suggested the cross-sectional amination levels were statistically the same at the 95% confidence level (exact two-tailed $p = 0.3498$). The Kolmogorov–Smirnov test also indicated they were statistically the same (approximate $p = 0.1417$).

This detailed Raman analysis shows that there were slight differences in the surface amination levels between MPIP(LEX) and MPIP(1.1). However, both RG-AEMs appear chemically the same when through-core amination levels are compared.

Solid-state NMR characterisation

$^{13}C\{^1H,^{19}F\}$ CP-MAS NMR was employed on samples of each RG-AEM to confirm grafting and amination,[7,18] and to investigate if there were any noticeable bulk changes in chemistry on using the different amination methods (Fig. 4). For the ETFE films, the C–F groups give a peak at 119 ppm and the C–H groups give peaks at 21 and 30 ppm (the latter due to amorphous polyethylene chains).[18–20] The grafting of the poly(VBC) chains onto the ETFE leads to additional peaks as reported previously:[18] CH and CH_2 groups in the aliphatic backbones of the graft poly(VBC) chains (41 ppm), the benzyl–CH_2Cl group (47 ppm), the quaternary aromatic carbons attached to the aliphatic backbones and the –CH_2Cl group (147 and 137 ppm, respectively), and the remaining aromatic carbons (129 ppm). On amination with *N*-methylpiperidine with both amination methods, the peak at 137 ppm disappears (possibly merges with the 129 ppm peak), a peak is observed at 45 ppm (that is lower in intensity compared to the adjacent peak at 41 ppm), and a group of indistinct peaks appear between 55–73 ppm. These spectral features match previous reports (see Fig. 4 in ref. 7) and confirm the formation of MPIP chemistry in the RG-AEMs.

It is clear from Fig. 4 that the ^{13}C spectra for both RG-AEMs are smilar within the noise. As with the Raman data, there is no evidence of large differences between the bulk chemistries of the two RG-AEMs made with the different amination procedures (consistent with the through-core Raman data above). The $^{15}N\{^1H\}$ CP-MAS spectra of both RG-AEMs displayed a single weak peak at −324 ppm, which again matches previously published data and confirms the presence of the MPIP groups.[7]

The $^{19}F\{^1H\}$ DP-MAS NMR spectra of ETFE (as supplied), ETFE-*g*-poly(VBC) and both RG-AEMs are presented in Fig. 5. As there are no F atoms in the grafted chains, this data is useful to monitor for any chemical or morphological changes (*e.g.* crystallinity – smaller linewidths stem from increased mobility of the polymer component) in the ETFE constituent at each stage in the synthesis. The five diagnostic peaks are assigned as follows:[20,21] −117, −123, and −131 ppm relate to CF_2 in –CH_2-$CH_2CF_2CF_2CH_2CH_2$–, –$CH_2CH_2CF_2CF_2CF_2CF_2CH_2CH_2$–, and terminal –$CF_2H$ groups (of termonomeric units) environments respectively; the small band at −83 ppm relates to –CF_3 groups in an additional component in the commercial film formulation; the broad peak at −75 ppm is also due to an additional F-containing component that may be specific to Nowflon (it does not appear in the ^{19}F spectrum of Dupont ETFE). There are no significant chemical or morphological changes when ETFE is irradiated and then grafted with VBC. There are observable differences in the ^{19}F peaks on amination of the ETFE-*g*-poly(VBC) membrane. However, the spectra of MPIP(LEX) and MPIP(1.1) are comparable suggesting the different amination

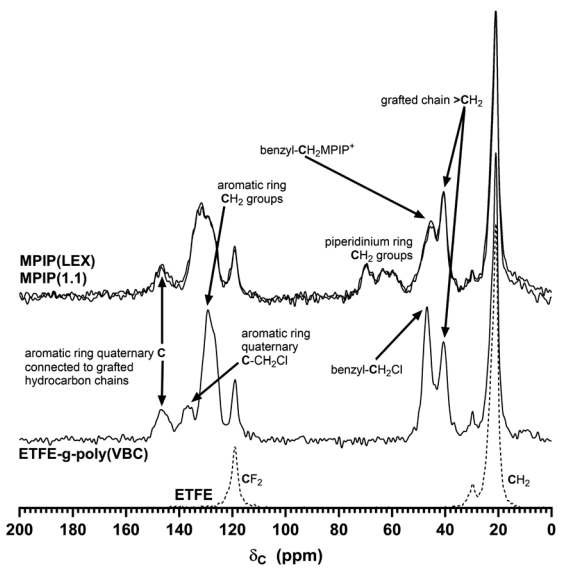

Fig. 4 $^{13}C\{^1H,^{19}F\}$ CP-MAS solid-state NMR spectra of ETFE, ETFE-*g*-poly(VBC), MPIP(LEX) and MPIP(1.1). Assignments from ref. 7.

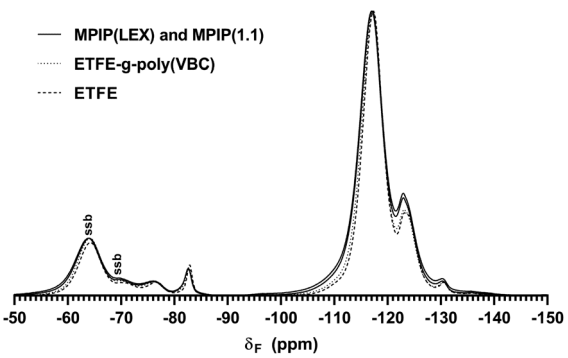

Fig. 5 $^{19}F\{^1H\}$ DP-MAS solid-state NMR spectra of ETFE (dashed), ETFE-*g*-poly(VBC) (dotted), MPIP(LEX) and MPIP(1.1) (solid). ssb = spinning sideband.

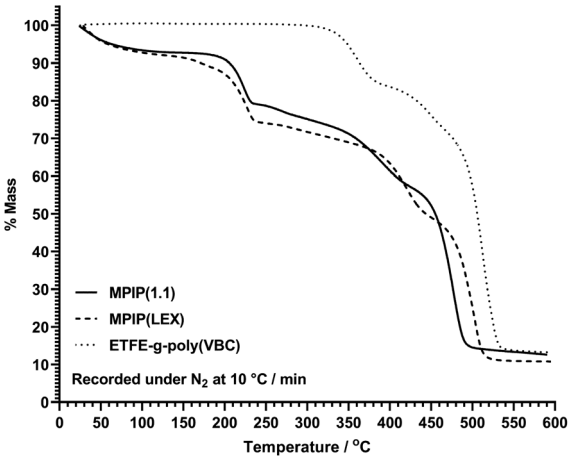

Fig. 6 The thermogravimetric analysis (TGA) of MPIP(1.1) and MPIP(LEX) and ETFE-*g*-poly(VBC) (DoG = 73%) recorded under flowing N_2 with a heating rate of 10 °C.

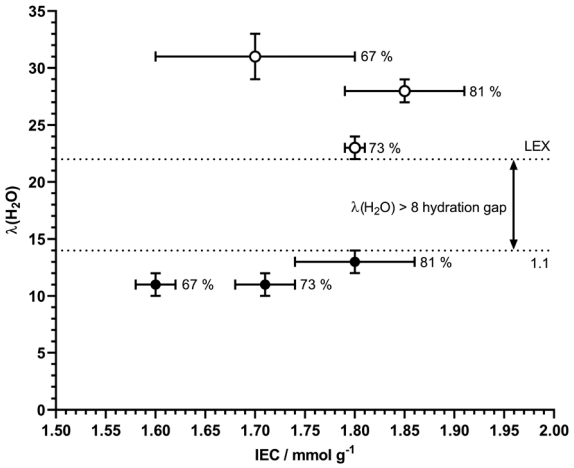

Fig. 7 The relationship between the water contents and IEC for all six Cl^- form RG-AEMs fabricated in this study (key properties presented in Table 1). The numbers to the right of the error bars are the degrees of grafting (DoG) of the ETFE-*g*-poly(VBC) grafted batch that was aminated with the two methods (LEX and 1.1).

methods do not leading to significant differences in the chemistry or morphology of the ETFE constituent.

Thermogravimetric analysis (TGA) in N_2

The TGA analysis of ETFE-*g*-poly(VBC), MPIP(LEX) and MPIP(1.1) is shown in Fig. 6. The initial mass loss for both RG-AEMs is due to loss of residual water. The mass loss between 125–240 °C is due to the presence of cationic MPIP groups as no mass loss is observed below 300 °C for the pre-aminated ETFE-*g*-poly(VBC) membrane (where loss of grafted chains commences around 310 °C). The final mass loss is predominantly due to residual ETFE (e^--beamed ETFE yields a single degradation event with an onset temperature of 400 °C – see ESI Section C Fig. S2†).

Despite the similar initial mass losses due to water content (note, the RG-AEMs would have dehydrated on handling and instrument loading to an uncontrolled degree), the onset of degradation of MPIP(LEX) above 120 °C is more rapid than for MPIP(1.1). Such a subtly different degradation profile is an initial indication that the two RG-AEMs are behaving differently.

Ion-exchange capacity and hydration properties (Cl^- forms)

The data presented in Table 1 shows that the IEC of MPIP(1.1) is 5% lower than the IEC of MPIP(LEX) suggesting that the level of amination is slightly lower for the RG-AEM made with a controlled, small excess of amine. This compares to the 1% (through-core) and 4% (surface) lower mean intensities of the 705 cm^{-1} MPIP-derived Raman band (normalised to the various ETFE bands) as discussed above. Additionally, on the switch to the 1.1 controlled excess amination method, a significant decrease in the water content (and dimensional swelling) was observed. The water contents are >50% lower for MPIP(1.1), which is a surprisingly large effect considering the smaller 5% reduction in IEC. This reduction in water content could have an impact when the RG-AEMs are applied in electrochemical cells such as CO_2RR cells (see later discussions).

Switch to RG-AEMs made from batch 2 and batch 3 of ETFE-*g*-poly(VBC) to enable further experiments

As there are natural variations between ambient condition gravimetric water uptakes recorded on different days, on top of the precision limits of the experiments being conducted, 2 further repeat batches of both the 1.1- and LEX-variants were fabricated and characterised to check the repeatability of the above IEC and water uptake observations (summarised in Fig. 7). A new batch of ETFE-*g*-poly(VBC) was grafted (yielding a DoG = 67%) and aminated using both methods: the resulting RG-AEMs are designated MPIP(LEX)-B2 and MPIP(1.1)-B2, with key properties summarised in Table 1. Due to the lower DoG, the IECs of the new batch of RG-AEMs were *ca.* 6% lower. It was clear that the water contents of MPIP(1.1)-B2, made with the smaller excess of *N*-methylpiperidine, was lower than MPIP(LEX)-B2. By directly comparing MPIP(LEX)-B2 to MPIP(1.1), where both have IECs = 1.7 mmol g^{-1}, it can be seen that MPIP(LEX)-B2 has a substantially higher water content: $\lambda(H_2O) = 31 \pm 2$ *vs.* 11 ± 1. A further batch 3 of ETFE-*g*-poly(VBC) was fabricated (DoG = 81%) to allow for more in-depth characterisations and for CO_2RR cell testing (key properties again summarised in Table 1). This batch 3 data further reinforces the finding that RG-AEMs exhibit higher water contents when made with a large excess of *N*-methylpiperidine.

All three MPIP(LEX)-batches exhibited $\lambda(H_2O) > 22$, which are all higher than the $\lambda(H_2O) < 14$ for the three MPIP(1.1)-batches (see Fig. 7). All of this strengthens the hypothesis that the differences in hydration, between RG-AEMs made using the different amination methods, is more fundamental than simply being due to small differences in IEC.

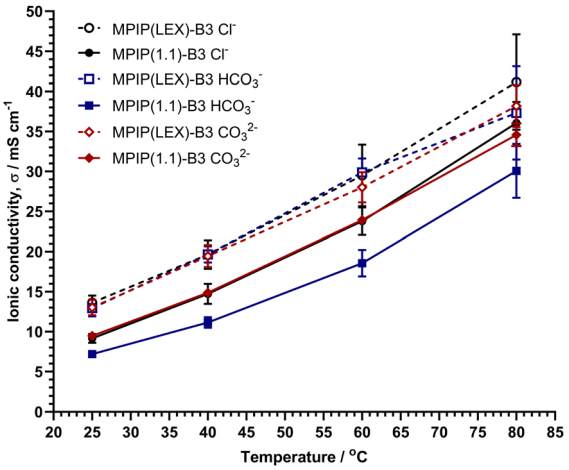

Fig. 8 The 4-probe (in-plane) conductivities of MPIP(LEX)-B3 (dashed) and MPIP(1.1)-B3 (solid) when submerged in water (fully hydrated) after ion-exchange in aqueous solutions containing Cl^- (black circles), HCO_3^- (blue squares), and CO_3^{2-} (red diamonds). Errors are sample standard deviations from measurements on $n = 3$ samples of each RG-AEM (some error bars are smaller than the symbols).

Table 2 Activation energies (E_a) estimated from the conductivities of the batch 3 RG-AEMs presented in Fig. 8

E_a/kJ mol^{-1}[a]	MPIP(LEX)-B3	MPIP(1.1)-B3
Cl^-	18	22
HCO_3^-	17	23
CO_3^{2-}	17	21

[a] Assuming a simple Arrhenius relationship (E_a values are extracted from the slopes of ln(σ) *vs.* $1/T$ data as previously reported).[11]

Anion conductivities of batch 3 RG-AEMs submerged in UPW

Fig. 8 shows that the higher water content MPIP(LEX)-B3 had higher conductivities compared to MPIP(1.1)-B3 over all temperatures. There is generally more intra-RG-AEM variance over different samples of MPIP(LEX)-B3 compared to MPIP(1.1)-B3. The conductivities of MPIP(1.1)-B3 that had been ion-exchanged in aqueous HCO_3^- are lower than the conductivities of the original Cl^- form (as synthesised) and when ion-exchanged in aqueous CO_3^{2-}. Comparing the conductivities of an AEM in different anion forms can be complex as on top of the different relative ion mobilities in water (relative to the ion mobility of K^+ defined as 1.00: $OH^- = 2.69$, $Cl^- = 1.04$, $CO_3^{2-} = 0.94$, and $HCO_3^- = 0.61$), a change in anion could cause a change in intrinsic hydration and morphology of the hydrated ion-transport channels as well as pH (relative alkalinity $CO_3^{2-} > HCO_3^- > Cl^-$ meaning that an AEM ion-exchange in aqueous CO_3^{2-} will have more highly mobile OH^- anions present compared to an AEM ion-exchanged in aqueous HCO_3^-).

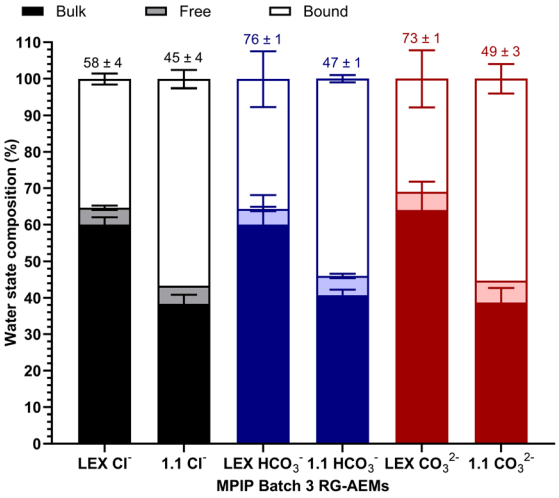

Fig. 9 THz-TDS measurements of the relative amounts of the states of water for MPIP(1.1)-B3 and MPIP(LEX)-B3 in different predominant anion forms. The numbers above each bar are gravimetric water contents recorded after transit to the Lancaster labs and after they had been re-hydrated at 20 °C for 24 h.

Estimated activation energies (E_a, from simple ln(σ) *vs.* $1/T$ Arrhenius analysis)[11] are higher for MPIP(1.1)-B3 compared to MPIP(LEX)-B3 for all anion-exchange forms (Table 2). All of this further suggests that the different amination methods are producing RG-AEMs that are fundamentally different. The ionic conductivity of ion-exchange membranes (IEM) is critical to performance in technologies such as fuel cells that operate at high current densities (>1.5 A cm^{-2}).[6] However, CO_2RR cells currently operate at lower current densities <1 A cm^{-2}.[2,22] A question that needs to be addressed: is conductivity or water diffusion rates more important for CO_2RR operation (see later discussions)?

THz-TDS investigation of the states of water (batch 3 RG-AEMs)

The water uptakes measurements independently conducted at Lancaster again re-confirm that they are higher for MPIP(LEX)-B3 compared to MPIP(1.1)-B3 (Fig. 9). However, knowing the proportions of the different water states is also useful. THz-TDS allows this as it accesses the electromagnetic spectrum between 0.1 and 3 THz, a higher frequency extension to that probed by microwave dielectric relaxation spectroscopy;[23,24] this coincides with the picosecond time-scales of water dipole dielectric relaxations (*e.g.* bulk water relaxation at 8 ps (ref. 23, 25 and 26) and free/fast water relaxation at <0.1 ps (ref. 25)). Water portions are then be determined by fitting the dielectric response of hydrated membranes using the double Debye model.[12,25,26]

The THz-TDS data shows that the MPIP(LEX)-B3 contains proportionately more bulk water (compared to bound and free water) compared to MPIP(1.1)-B3 in all anions forms. Bound water is where hydrogen-bonded H_2O water molecules are strongly associated with the (ionic or polar) functional groups on an IEM's polymer backbone, bulk water is the H_2O molecules that exhibit co-operative reorganisation of hydrogen bonds with

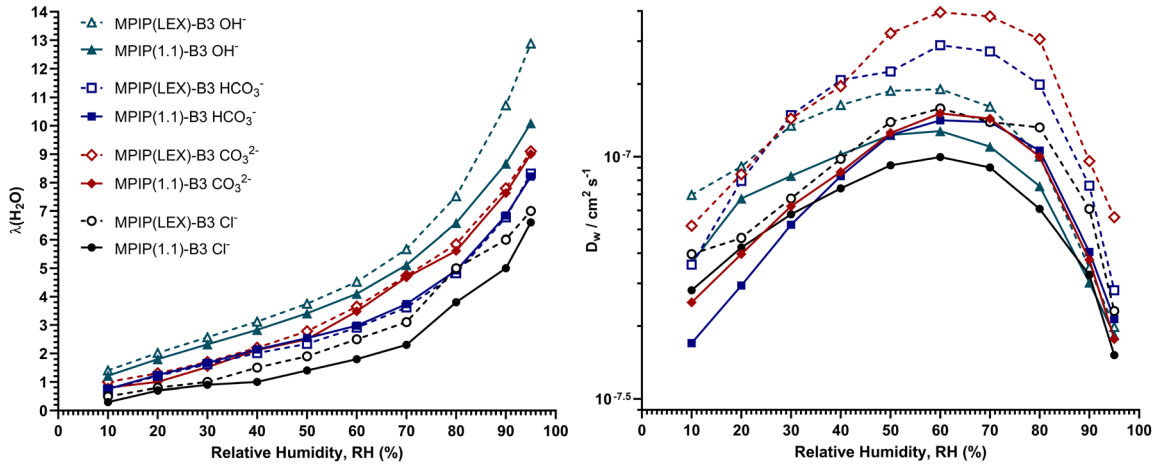

Fig. 10 The water contents $\lambda(H_2O)$ (left hand plot) and water diffusion coefficients (D_w) (right hand plot) at 25 °C measured as batch 3 dehydrated RG-AEM samples (in all predominant anion forms) were hydrated in steps in N_2 atmospheres containing increasing relative humidities (RH).

weaker interactions with the polymer chains, and free water is the water molecules with no significant interaction with the polymer chains.[12] An increase in bulk water is generally associated with the formation of channels of hydrogen-bonded water that can combine isolated hydrophilic ionic domains resulting in a continuous network, which in turn promote water diffusion and enhance ion conduction. Interestingly, the predominant anion present does not significantly change the relative proportions of the three different states of water (at least for Cl^-, HCO_3^- and CO_3^{2-}), but this could be due to the limited sensitivity of the present state of development of this new technique where the measurements are recorded under ambient conditions.

Dynamic vapour sorption (DVS) experiments (batch 3 RG-AEMs)

The batch 3 RG-AEMs were evaluated in the predominant Cl^-, HCO_3^-, and CO_3^{2-} forms, as well as the OH^- forms (Fig. 10). The latter was studied because of the significantly higher water contents and ion conductivities exhibited compared to other anion forms.[27,28] The data in Fig. 10 reconfirms the higher water contents of the OH^- forms: at RH > 50%, $\lambda(H_2O)$ generally increases $Cl^- < HCO_3^- < CO_3^{2-} < OH^-$.

It is clear that the water diffusion coefficients (D_w) is higher for MPIP(LEX)-B3 compared to MPIP(1.1)-B3 for all anion forms across the whole range of RHs tested. At RH = 60%, D_w decreases in the order $CO_3^{2-} > HCO_3^- > OH^- > Cl^-$. Despite having higher $\lambda(H_2O)$ values, D_w values get smaller (slower) at higher RHs, especially for OH^- forms, due to larger size of water clusters formed inside the AEMs resulting in slower mobility. The D_w values obtained were from measurement of the relaxation time of water mobility from the membrane/water vapour interface through the thickness of RG-AEM sample. As water activity increases, $\lambda(H_2O)$ increases and the proportion of free water unbounded (to anions) increases, forming clusters with increased size. Water initially nucleates in the hydrophilic

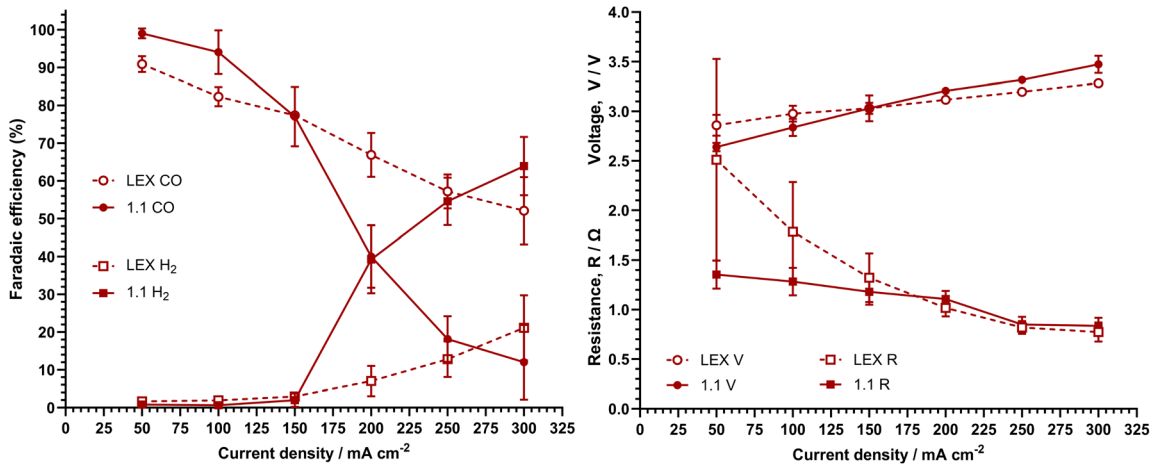

Fig. 11 Room temperature galvanostatic CO_2RR cell test data for MPIP(1.1)-B3 and MPIP(LEX)-B3 (2.25 cm^2 geometric electrode area). The cathode was Ag-based supplied with 30 mL min^{-1} dry CO_2. The anode was IrO_2-based supplied with aqueous $KHCO_3$ (0.1 mol dm^{-3}) supplied at 40 mL min^{-1}. Voltage and resistance data was collected at constant currents with resistances collected using the current interrupt method. Error bars are from $n = 3$ repeat cell tests with different samples of each AEM. ESI† contains anode data.

regions then penetrates more into the hydrophobic regions where water clusters grow quickly. The mobility of the clusters decreases with increase in their size (and mass). This has been observed in a range of polymers[29] and more recently in COFs.[30]

For both RG-AEMs tested, the CO_3^{2-} and HCO_3^- forms have higher D_w at the higher RHs compared to the OH^- forms, but lower D_w at lower RHs. For MPIP(LEX)-B3, the Cl^- anion form also has a higher D_w at RH > 80% compared to the OH^- form. This crossover behaviour has been previously reported for Tokuyama A201 AEM (using pulse field gradient NMR experiments), where water self-diffusion is higher for the OH^- form at lower $\lambda(H_2O)$ values (*cf.* the HCO_3^- forms), but lower at higher $\lambda(H_2O)$ values.[28]

CO_2RR cell testing (batch 3 RG-AEMs)

Fig. 11 shows CO_2 electrolysis performance of MPIP(1.1)-B3 and MPIP(LEX)-B3 (galvanostatic discharge data). In these tests, the catalysts were the same (Ag cathode, IrO_2 anode) thus the results are purely a relative comparison of CO_2 to CO electrolysis for the specific RG-AEMs tested. At higher current densities, undesired selectivity to HER is higher for the MPIP(1.1)-B3 samples compared to the analogous MPIP(LEX)-B3 samples, while both RG-AEMs yielded the same *in situ* ohmic resistances. This highlights the importance of facile water transport in such cells, as the MPIP(LEX)-B3 could clearly maintain higher CO selectivities at the higher current densities due to this improved water management (recall the higher D_w values in Fig. 10).

The anodic performance data (shown in the ESI Section B in Fig. S1†) also contains the anode CO_2/O_2 gas production ratios. This ratio ranged between 1.7–2.8 indicating that CO_3^{2-} anions are the predominant conductive species through the AEMs (ratios of 0, 2, and 4 indicate predominant OH^-, CO_3^{2-}, and HCO_3^- conduction, respectively).[4]

In the low current density region (<150 mA cm^{-2}), and compared to MPIP(LEX)-B3, we observed that MPIP(1.1)-B3 operated at a lower cell voltage, even though the catalysts are identical, and produced lower *in situ* resistances. A plausible

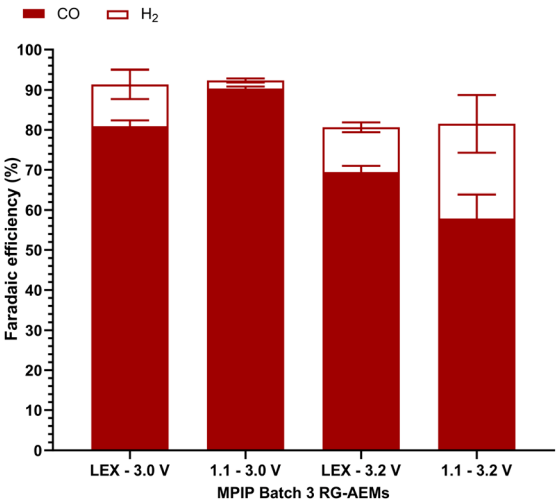

Fig. 13 The CO and H_2 faradaic efficiencies collected at the end of the room temperature potentiostatic CO_2RR cell tests in Fig. 12.

hypothesis is that this is due to the lower water contents in MPIP(1.1)-B3. Lower water uptake means OH^- anions produced *via* the CO_2 electrolysis half reaction will be up-concentrated at the cathode leading locally to a higher pH environment. Since more alkaline environments lowers ohmic resistances (OH^- are more conductive than the other anions),[31] this could be a reason for lower cell potentials. The CO_2/O_2 ratio is slightly higher for the MPIP(LEX)-B3 compared to the MPIP(1.1)-B3 (shown in the ESI Section B in Fig. S1†), giving some basis for this explanation.

Constant potential experiments were also conducted at 3.0 V and 3.2 V (Fig. 12). Only the first 60 s was shown as the focus was on the equilibrated current density rather than other issues such as RG-AEM degradation, which is outside the scope of this work. At both potentials, MPIP(1.1)-B3 produced higher current densities (*cf.* MPIP(LEX)-B3) even though it also yielded higher ohmic resistances; the higher performance was much more pronounced at 3.0 V compared to 3.2 V. This supports the

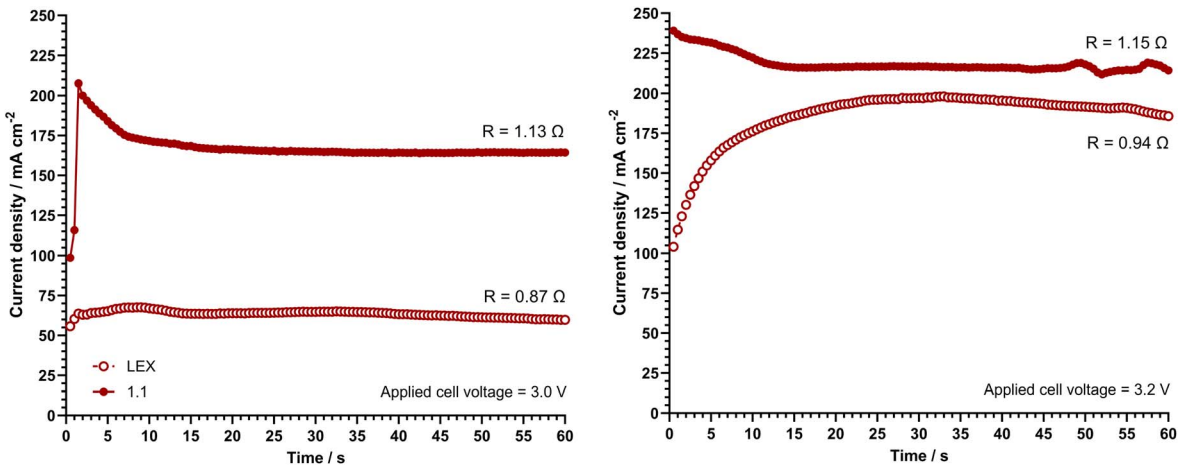

Fig. 12 Room temperature potentiostatic CO_2RR cell test data for MPIP(1.1)-B3 and MPIP(LEX)-B3 (2.25 cm^2 geometric electrode area). The cathode was Ag-based supplied with 30 mL min^{-1} dry CO_2. The anode was IrO_2-based supplied with aqueous $KHCO_3$ (0.1 mol dm^{-3}) supplied at 40 mL min^{-1}.

aforementioned hypothesis, since catalysis plays a less dominating role in performance at larger potentials compared to ohmic and mass transfer losses. Note, this is an initial and speculative hypothesis and localized mass transfer models would be needed for validation. However, this observation was made possible due to the fabrication of near identical chemistry RG-AEMs with different water contents.

As higher CO faradaic efficiencies are achieved at 3.0 V with both batch 3 RG-AEMs (Fig. 13), the slightly higher efficiency with MPIP(1.1)-B3 is likely just a function of the low current density and there being no CO_2 mass transport limitations. Once this is taken to higher current densities (*via* higher voltages), the drop in CO selectivity of MPIP(1.1)-B3 could indicate localised mass transport issues or minor H_2 generation due to a HER contaminant such as Ni. At the higher current densities we see little change in the HER with MPIP(LEX)-B3 compared to a substantial increase in HER with MPIP(1.1)-B3.

As mentioned in the preceding study,[10] that down-selected the ETFE-based MPIP-type over other types of RG-AEM, CO_2RR cell performances are comparable to commercial types such as Sustainion XC-72 (Dioxide Materials USA), PiperION (Versogen USA), and FAA-3-50 (Fumatech GmbH, Germany). This is summarised in Fig. 4 in ref. 10 and repeated here for context. For example, at the comparison point of 150 mA cm^{-2} with CO2RR cells operated at room temperature (Fig. 11), the faradaic efficiency for CO production (FE(CO)) with the batch-3 MPIP-AEMs was (77 ± 8) % with <3% FE(H_2); this compares to FE(CO) of (84 ± 3) % with Sustainion XC-72, (86 ± 3) % with PiperION, and (64 ± 6) % with FAA-3-50 when comparison tested in the same cell set-ups. As an aside, this prior study also presented a comparison between an MPIP-AEM and Sustainion XC-72 regarding CO_2RR performances at 60–80 °C (Fig. 5 in ref. 10). This showed that the MPIP-based RG-AEM formulation can give highly competitive performances (FE(CO) > 50% and <5% for MPIP-AEM and Sustaintion at 80 °C, respectively).

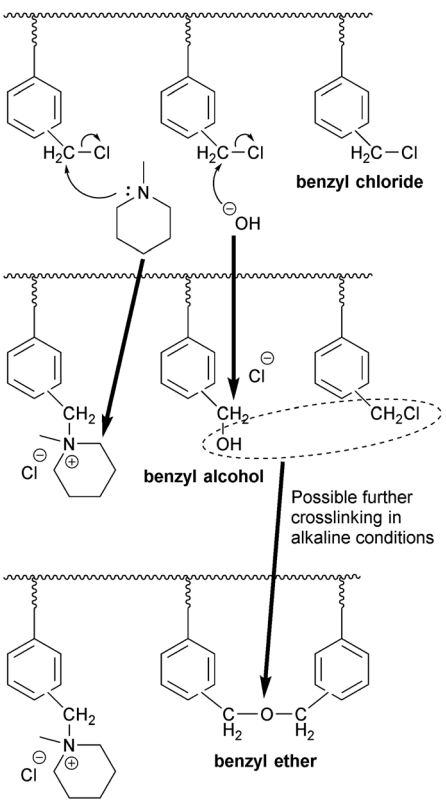

Scheme 2 A reaction between benzyl chloride groups and mixtures of *N*-methylpiperidine and OH^- anions (hypothesis 2 discussed in the main text).

Investigation into the cause of the lower water uptakes with the use of 1.1 excess of *N*-methylpiperidine

We now consider the possible hypotheses for the lower water contents of the MPIP(1.1)-batches compared to the analogous MPIP(LEX)-batches.

Hypothesis 1. Is the differing water content behaviours down to chemical changes in the partially fluorinated ETFE component, due to the combination of high energy e^--beam treatment and exposure to the differing *N*-methylpiperidine solutions (the aqueous 15 vol% *N*-methylpiperidine solution is pH = 12.4, while the *N*-methylpiperidine solution used to make the MPIP(1.1)-versions is pH = 11.6)? This hypothesis was deemed unlikely for several reasons. Firstly, the same trend was observed when the MPIP-based RG-AEMs were made from e^--beamed (non-fluorinated) HDPE precursor films (see ESI Section A†), so this effect is not a function of the precursor film used. Secondly, ^{13}C NMR, ^{19}F NMR, Raman, and TGA data showed that there were no detectible differences between e^--beamed ETFE films that were not grafted but were exposed at 60 °C to the two different aqueous *N*-methylpiperidine solutions used to make the MPIP(1.1)- and MPIP(LEX)-batches (see ESI Section C†).

Hypothesis 2. As the aqueous *N*-methylpiperidine solution used to make the MPIP(1.1)-batches is lower in concentration than that used to make the MPIP(LEX)-batches, this leads to the following question: could the reaction of *N*-methylpiperidine with the benzyl chloride groups in the ETFE-*g*-poly(VBC) membranes be slower in the former case (lower *N*-methylpiperidine concentration), resulting in more time for some of the $-CH_2Cl$ groups to react with the nucleophilic OH^- anions, that are present in the aqueous alkaline amine solution, leading to the formation of more polar, but uncharged, benzyl alcohol groups ($-CH_2OH$, Scheme 2). These benzyl alcohol groups do not contain a good enough leaving group to further react with the tertiary nitrogen in the *N*-methylpiperidine molecules, so the formation of such $-CH_2OH$ groups would lower the IECs of the resultant RG-AEMs (as they have taken up $-CH_2Cl$ groups that will not be converted into positively charged QA groups with associated mobile anions); this is observed for the MPIP(1.1)-batches (IEC comparisons in Table 1).

A prior study,[32] that discusses Raman and IR spectra of benzyl alcohol ($PhCH_2OH$), indicates that a COH bending band is expected at 700 cm^{-1}, while a CH_2 bending band is expected at 1160 cm^{-1}. Reaction of a sample of ETFE-*g*-poly(VBC) at 60 °C with *N*-methylpiperidine in aqueous KOH led to the appearance of an intense, broad band at 1161 cm^{-1} (see ESI Section D†),

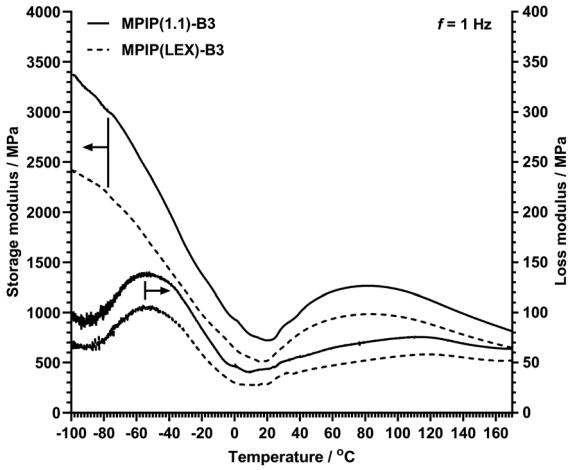

Fig. 14 Dynamic mechanical analysis (DMA) data obtained with samples of MPIP(LEX)-B3 and MPIP(1.1)-B3 (where each trace is an average of data collected on $n = 3$ samples of each RG-AEM in the Cl^- forms).

which was not visible in the control sample (aminated with *N*-methylpiperidine in UPW). Examination of the Raman spectra presented in Fig. 2 does not show any major differences between MPIP(1.1) and MPIP(LEX) in these spectral regions, so if such OH^- attack of the benzyl chloride groups is occurring, it is happening to an extent that is below such spectral detection (lots of bands overlapping in these regions).

The benzyl alcohol groups also have the potential to react with adjacent $-CH_2Cl$ groups in alkali environments to form ether crosslinks (bottom of Scheme 2). The replacement of some of the positively charged MPIP groups with either short crosslinks or uncharged (but hydrogen-bonding) groups would be expected to have a dramatic effect on hydration levels and the relative states of water in the RG-AEMs, as was observed and discussed above (*e.g.* Fig. 7 and 9). Crosslinking typically lowers water contents and conductivities.[16] The presence of crosslinks or covalently bound hydrogen-bonding groups would also be expected to make the RG-AEM stiffer. DMA data (Fig. 14) shows that MPIP(1.1)-B3 is generally stiffer than MPIP(LEX)-B3, which provides possible indirect evidence of this hypothesis. Note, the DMA traces in Fig. 14 are non-standard in shape due to the presence of residual water in the RG-AEMs (mounted without hydration control), which can freeze or evaporate to produce modulus changes in parallel to the normal thermal transitions, such as the glass transition temperature (T_g).

Hypothesis 3. The different amination procedures leads to non-chemical differences between the RG-AEMs, such as different nano-morphologies or crystallinities. To probe this hypothesis, small angle scattering experiments (SAXS and SANS) were conducted to determine the characteristic sizes of lamellar structures, which in such systems consist of lamella crystalline and amorphous layers within stacked lamellae, as previously reported.[33–37] Analysis of the SAXS and SANS profiles of batch 3 RG-AEMs (Fig. 15) indicates the presence of three regions:

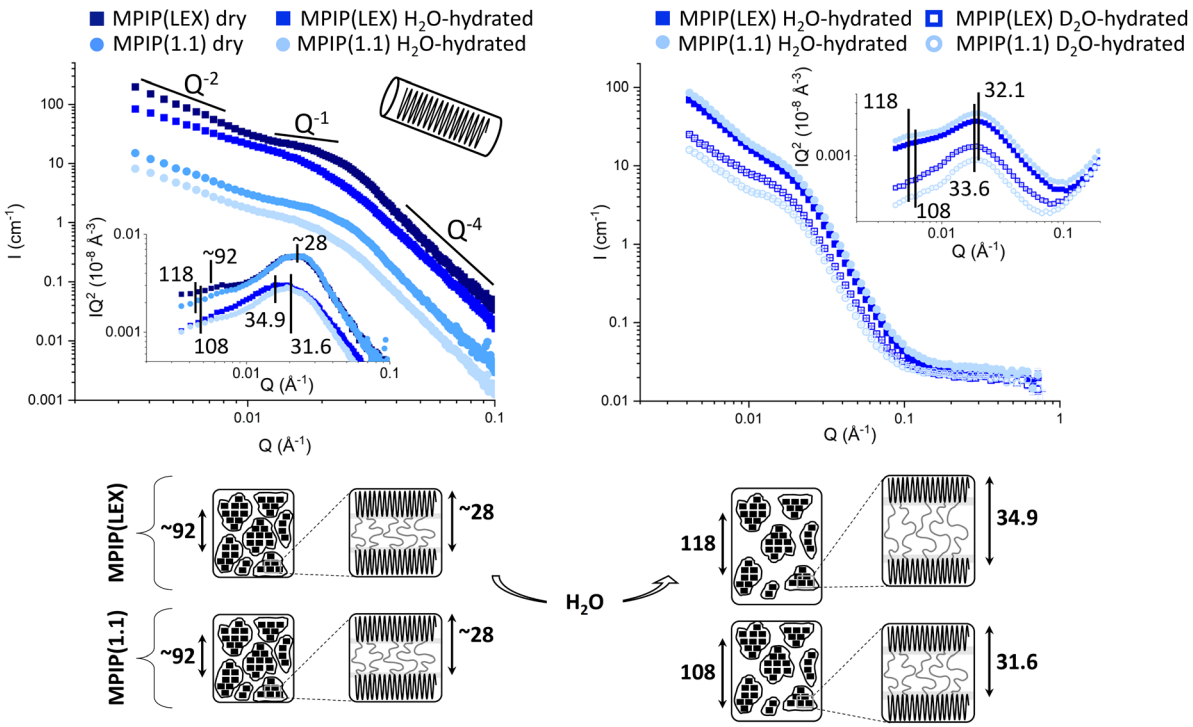

Fig. 15 SAXS (left panel) and SANS (right panel) profiles for MPIP(LEX)-B3 and MPIP(1.1)-B3 (square and circle symbols; respectively) in their dry and fully hydrated (H_2O and D_2O open black and grey symbols; respectively). In the inset profiles give Lorentz-corrected data, to highlight the feature at low-*Q*. The cartoon in the plot represents the geometry of the crystalline domains as evaluated by the slope (*e.g.* Q^{-1}). At the bottom is presented a cartoon explicating the domain size (nm) and their relative swelling.

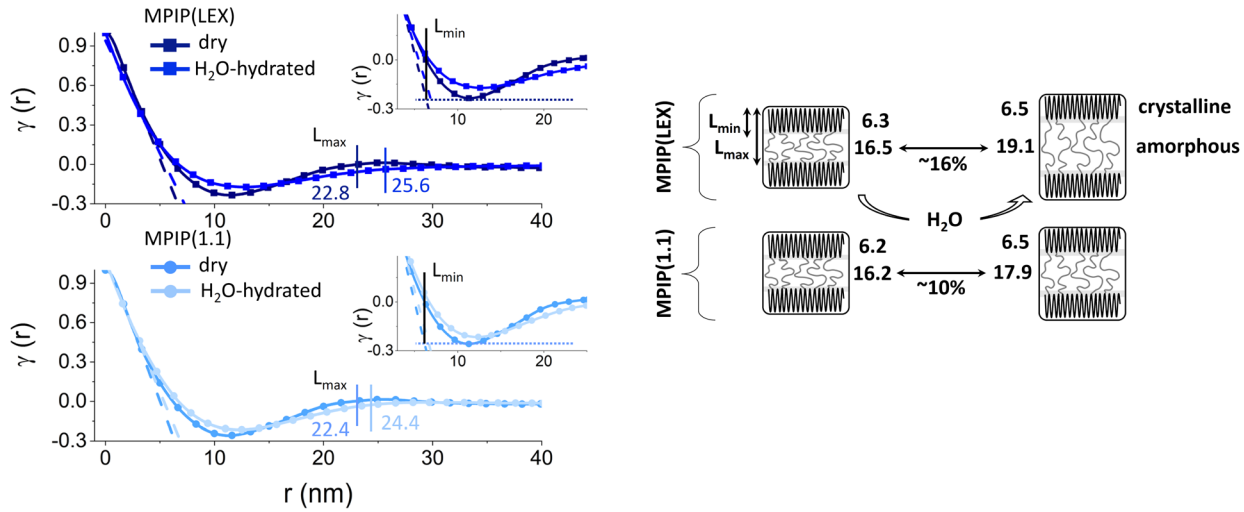

Fig. 16 1D Correlation function for MPIP(LEX)-B3 and MPIP(1.1)-B3 (square and circle symbols; respectively) in their dry state. In the inset highlights L_{min} and L_{max}. At the bottom is a cartoon explicating the domain size (nm) and their relative swelling.

region I ($0.03 \leq Q \leq 0.3$ Å^{-1}) characterized by a power law $I(Q) \sim Q^{-4}$, attributed to a sharp interface between amorphous and crystalline domains;[33,35,38]

region II (centred around $Q = 0.016$ Å^{-1}; $I(Q) \sim Q^{-1}$), indicating that the crystalline lamellar domains are rod-like;[33,35]

region III ($0.0035 \leq Q \leq 0.012$ Å^{-1}; $I(Q) \sim Q^{-2}$), typical for disk-like and/or lamellar structure.

To highlight the signal in the low-Q region, which reflects the large length scale morphology, and originates from the variations in the crystallites and the amorphous phases, Lorentz-corrected profiles were also presented ($I(Q)Q^2$ *vs.* Q; insets to Fig. 15). Here, the estimation of the structural dimension (d-spacing $= 2\pi/Q$) allows us to evaluate not only the lamellar thickness but also the correlation length between orientated crystallites.[33] Although the three zones are present in both RG-AEMs, the measurement of these distances before and after hydrating the samples indicates that various amination processes result in an alteration of RG-AEM nano-morphology. More precisely, it appears to have an impact on the size of the amorphous layer and the oriented crystallite interspace: *e.g.* a 40% difference in swelling between MPIP(LEX)-B3 and MPIP(1 : 1)-B3, which is consistent with the TPS data presented in Table 1. Afterall, the grafted polymer chains, and hence the component that is aminated and most affected by changes in the amine concentration used, are mainly located in the amorphous domains of RG membranes (the radiation induced radicals in the crystallite domains migrate to the crystallite–amorphous interfaces where they initiate copolymerisation into the amorphous domains).[39]

The 1D correlation function $\gamma(r)$ has also been assessed to gain more understanding of the lamella stacking structure (Fig. 16). With the latter, it is possible to estimate the relative thickness of crystalline and amorphous layers (assuming randomly oriented layers):[38,40]

$$\gamma(r) = \frac{\int_0^\infty I(Q)Q^2\cos(Qr)\mathrm{d}Q}{\int_0^\infty I(Q)Q^2\mathrm{d}Q} \quad (12)$$

The analysis of the 1D correlation function from the SAXS data indicates that amination affects the amorphous layer's swelling capacity even while the crystalline layer is essentially unaffected. The difference in swelling in this specific instance is about 33%, which is only slightly lessened when compared to the large-scale swelling (Table 1 TPS data).

Conclusions

A series of ETFE-based radiation-grafted anion-exchange membranes (RG-AEMs) containing the *N*-benzyl-*N*-methylpiperidnium (MPIP) headgroup chemistry were fabricated for potential use in electrochemical CO_2 reduction cells (CO_2RR). Traditionally such RG-AEMs were fabricated using a large excess of *N*-methylpiperidine amine reagent, but to reduce the chemical waste involved, a new fabrication protocol was trialled, where only a 1.1 excess of amine was used.

Raman and NMR spectroscopic evidence initially indicated that the new amination protocol was successful, where only subtle differences in RG-AEM chemistry could be detected. However, the new amination protocol led to repeatable reductions in ion-exchange capacities (IEC), along with a lowering of anion conductivities, a notable reduction in water contents, including a smaller proportion of bulk water, and slower water diffusion dynamics. This shows that the physical properties of the RG-AEMs made using the new 1.1 amination stoichiometry protocol were significantly different compared to the RG-AEMs made using the traditional large excess of amine. This resulted in altered *in situ* behaviours in a CO_2RR cell (Ag cathode, $CO_2 \rightarrow$ CO performance).

X-ray and neutron scattering experiments clearly show that the different levels of swelling on hydration, observed when the RG-AEMs were made using the new 1.1 protocol, is due to changes in nano-morphological responses of the amorphous lamella regions in the RG-AEM. Alongside the aforementioned reductions in IEC, and when also considering that the new protocol produced higher modulus RG-AEMs, this all suggests there may be additional formation of benzyl alcohol groups

(hydrogen bonding) and/or crosslinking side reactions occurring with the new 1.1 amination protocol. This would be consistent with the observed poorer water and ion dynamics, and the reduction in swelling on hydration (at both the bulk and nanoscopic scales). It is also consistent with the more rapid onset of polymer degradation seen in the thermogravimetic analysis of the slightly higher IEC RG-AEM fabricated using the traditional excess amine protocol (benzyltrimethyl ammonium groups are expected to be less thermally stable than uncharged headgroups and crosslinks).

This study shows that changes in AEM fabrication procedures, while only leading to minor changes in their chemistries, can yield more significant changes in their nano-morphological, physical, and technological application relevant behaviours. This represents an important insight that is of potential interest to researchers who either develop or use ion-exchange membranes.

Conflicts of interest

There are no conflicts to declare.

Author contributions

University of Surrey: Terry Willson fabricated the RG-AEMs and collected the Raman spectro-microscopic and Cl^- form physical property data presented in Fig. 1–3, 7, and 14, and Table 1; he was also originator of the idea to look at the different amination methods. John Varcoe led the coordination of the paper, and contributed to data analysis and visualisation, researcher supervision, and the drafting of the bulk of the manuscript. Ihtasham Salam collected the thermal analysis data presented in Fig. 6. Arun Periasamy collected the conductivity data presented in Fig. 8. Daniel Whelligan contributed to researcher supervision, manuscript drafting, data analysis and ideas for the differing water contents with the different amination methods. UCL/STFC-ISIS: scattering experiments were directed and interpreted by Fabrizia Foglia; scattering profiles were acquired in collaboration with Keenan Smith and Najet Mahmoudi. DTU: Carlos Giron Rodriguez did the CO_2 electrolysis experiments that generated the data in Fig. 11 and contributed to writing the section corresponding to this work. Similarly, Qiucheng Xu collected the data presented in Fig. 12 and 13. Brian Seger helped design experiments, analyse data, and edit the manuscript. Newcastle University: Ravikumar Ravikumar and Vinothkannan Mohanraj collected the DVS data presented in Fig. 10. Mohamed Mamlouk helped design experiments, analyse data, and edit the manuscript. Lancaster University: Jordan Frow collected and analysed the THz-TDS results presented in Fig. 9. Hungyen Lin contributed to researcher supervision, manuscript drafting and THz data analysis.

Acknowledgements

This research was primarily funded by the European Union's Horizon 2020 research and innovation programme under grant agreement no. 851441 (project SELECTCO2, led by DTU). The resources used for conductivity experiments were funded by the UK Engineering and Physical Sciences Research Council (EPSRC) grant EP/T009233/1. The Raman microscope was funded by EPSRC grant EP/M022749/1. We thank Dr Sam Page (Solid-state NMR Service, University of Durham) for recording the solid-state NMR spectra (data in Fig. 4 and 5). DTU would also like to acknowledge support from the Villum Foundation's VSustain center (project # 9455). The Lancaster team acknowledges support from EPSRC H_2FC Supergen Flexible Grant EP/P024807/1, the Royal Academy of Engineering for funding Dr Lin's Industrial Fellowship, the Centre for Global Eco-Innovation PhD Programme, Dr Riccardo Degl'Innocenti for THz-TDS equipment access, and discussions with Dr Gaurav Gupta. The Newcastle team's dynamic water sorption work were resourced from EPSRC grant EP/T00939X/1. The UCL team acknowledges EPSRC for funding (grants EP/V057863/1 and EP/W033321/1), ISIS (Harwell, STFC, UK) for neutron beamtime (**https://doi.org/10.5286/ISIS.E.RB2291004-1**), and gratefully acknowledge Dr Han Wu and the EPSRC CNIE research facility service (EPSRC Award, EP/S03305X/1) at University College London for assisting the collection of SAXS data. The University of Surrey also thanks Dr Friedrich Menges for granting a free licence for use of the Spectragryph software: **https://www.effemm2.de/spectragryph/index.html**.

References

1 D. A. Salvatore, C. M. Gabardo, A. Reyes, C. P. O'Brien, S. Holdcroft, P. Pintauro, B. Bahar, M. Hickner, C. Bae, D. Sinton, E. H. Sargent and C. P. Berlinguette, *Nat. Energy*, 2021, **6**, 339.
2 S. Garg, C. A. Giron Rodriguez, T. E. Rufford, J. R. Varcoe and B. Seger, *Energy Environ. Sci.*, 2022, **15**, 4440.
3 B. Endrődi, E. Kecsenovity, A. Samu, T. Halmágyi, S. Rojas-Carbonell, L. Wang, Y. Yan and C. Janáky, *Energy Environ. Sci.*, 2020, **13**, 4098.
4 M. Ma, E. L. Clarke, K. T. Therkildsen, S. Dalsgaard, I. Chorkendorff and B. Seger, *Energy Environ. Sci.*, 2020, **13**, 977.
5 Z. Yin, H. Peng, X. Wei, H. Zhou, J. Gong, M. Hai, L. Xiao, G. Wang, J. Lu and L. Zhuang, *Energy Environ. Sci.*, 2019, **12**, 2455.
6 L. Wang, X. Peng, W. E. Mustain and J. R. Varcoe, *Energy Environ. Sci.*, 2019, **12**, 1575.
7 J. Ponce-González, D. K. Whelligan, L. Wang, R. Bance-Soualhi, Y. Wang, Y. Peng, H. Peng, D. C. Apperley, H. N. Sarode, T. P. Pandey, A. G. Divekar, S. Seifert, A. M. Herring, L. Zhuang and J. R. Varcoe, *Energy Environ. Sci.*, 2016, **9**, 3724.
8 A. M. A. Mahmoud, K. Yoshimura and Y. Maekawa, *J. Membr. Sci.*, 2021, **620**, 118844.
9 **https://www.selectco2.eu/**.
10 C. A. Giron Rodriguez, B. O. Joensen, A. B Moss, G. O. Larrazábal, D. K. Whelligan, B. Seger, J. R. Varcoe and T. R. Willson, *ACS Sustainable Chem. Eng.*, 2023, **11**, 1508.

11 L. Wang, E. Maggliocca, E. L. Cunningham, W. E. Mustain, S. D. Poynton, R. Escudero-Cid, M. M. Nasef, J. Ponce-González, R. Bance-Soualhi, R. C. T. Slade, D. K. Whelligan and J. R. Varcoe, *Green Chem.*, 2017, **19**, 831.
12 D. F. Alves-Lima, X. Li, B. Coulson, E. Nesling, G. A. H. Ludlam, R. Degl'Innocenti, R. Dawson, M. Peruffo and H. Lin, *J. Membr. Sci.*, 2022, **647**, 120329.
13 O. Arnold, J. C. Bilheux, J. M. Borreguero, A. Buts, S. I. Campbell, L. Chapon, M. Doucet, N. Draper, R. Ferraz Leal, M. A. Gigg, V. E. Lynch, A. Markvardsen, D. J. Mikkelson, R. L. Mikkelson, R. Miller, K. Palmen, P. Parker, G. Passos, T. G. Perring, P. F. Peterson and J. Zikovsky, *Nucl. Instrum. Methods Phys. Res., Sect. A*, 2014, **764**, 156.
14 G. D. Wignall and F. S. Bates, *J. Appl. Crystallogr.*, 1987, **20**, 28.
15 A. L. G. Biancolli, D. Herranz, L. Wang, G. Stehlíková, R. Bance-Soualhi, J. Ponce-González, P. Ocón, E. A. Ticianelli, D. K. Whelligan, J. R. Varcoe and E. I. Santiago, *J. Mater. Chem. A*, 2018, **6**, 24330.
16 R. Bance-Soualhi, M. Choolaei, S. A. Franklin, T. R. Willson, J. Lee, D. K. Whelligan, C. Crean and J. R. Varcoe, *J. Mater. Chem. A*, 2021, **9**, 22025.
17 K. M. Meek, C. M. Reed, B. Pivovar, K.-D. Kreuer, J. R. Varcoe and R. Bance-Soualhi, *RSC Adv.*, 2020, **10**, 36467.
18 J. R. Varcoe, R. C. T. Slade, E. Lam How Yee, S. D. Poynton, D. J. Driscoll and D. C. Apperley, *Chem. Mater.*, 2007, **19**, 2686.
19 W. Pang, C. Fan and Q. Zhu, *Eur. Polym. J.*, 2001, **37**, 2425.
20 K. Aimi and S. Ando, *Magn. Reson. Chem.*, 2004, **42**, 577.
21 T. Isemura, Y. Jitsugiri and S. Yonemori, *J. Anal. Appl. Pyrolysis*, 1995, **33**, 103.
22 T. Möller, W. Ju, A. Bagger, X. Wang, F. Luo, T. Ngo Thanh, A. S. Varela, J. Rossmeisl and P. Strasser, *Energy Environ. Sci.*, 2019, **12**, 640.
23 Z. Lu, G. Polizos, D. D. MacDonald and E. Manias, *J. Electrochem. Soc.*, 2008, **155**, B163.
24 S. O. Yurchenko and K. I. Zaytsev, *J. Appl. Phys.*, 2014, **116**, 113508.
25 N. Devi, S. Ray, A. Shukla, S. D. Bhat and B. Pesala, *J. Membr. Sci.*, 2019, **588**, 117183.
26 K. J. Tielrooij, D. Paparo, L. Piatkowski, H. J. Bakker and M. Bonn, *Biophys. J.*, 2009, **97**, 2484.
27 T. P. Pandey, A. M. Maes, H. N. Sarode, B. D. Peters, S. Lavina, K. Vezzù, Y. Yang, S. D. Poynton, J. R. Varcoe, S. Seifert, M. W. Liberatore, V. Di Noto and A. M. Herring, *Phys. Chem. Chem. Phys.*, 2015, **17**, 4367.
28 J. Peng, A. L. Roy, S. G. Greenbaum and T. A. Zawodzinski, *J. Power Sources*, 2018, **380**, 64.
29 J. A. Barrie and B. Platt, *Polymer*, 1963, **4**, 303.
30 K. T. Tan, S. Tao, N. Huang and D. Jiang, *Nat. Commun.*, 2021, **12**, 6747.
31 S. Nitopi, E. Bertheussen, S. B. Scott, X. Liu, A. K. Engstfeld, S. Horch, B. Seger, I. E. L. Stephens, K. Chan, C. Hahn, J. K. Nørskov, T. F. Jaramillo and I. Chorkendorff, *Chem. Rev.*, 2019, **119**, 7610.
32 D. A. Prystupa, A. Anderson and B. H. Torrie, *J. Raman Spectrosc.*, 1994, **25**, 175.
33 T. D. Tap, S.-i. Sawada, S. Hasegawa, K. Yoshimura, Y. Oba, M. Ohnuma, Y. Katsumura and Y. Maekawa, *Macromolecules*, 2014, **47**, 2373.
34 T. D. Tap, P. M. Hien, N. H. Anh, L. T. Anh and L. A. Tuyen, *Sci. Technol. Dev.*, 2015, **18**, 153.
35 Y. Zhao, K. Yoshimura, H. Shishitani, S. Yamaguchi, H. Tanaka, S. Koizumi, N. Szekely, A. Radulescu, D. Richtere and Y. Maekawa, *Soft Matter*, 2016, **12**, 1567.
36 T. Duy Tap, L. L. Nguyen, Y. Zhao, S. Hasegawa, S.-i. Sawada, N. Q. Hung, L. A. Tuyen and Y. Maekawa, *Macromol. Chem. Phys.*, 2020, **221**, 1900325.
37 J. M. Song, B. S. Ko, J. Y. Sohn, Y. C. Nho and J. Shin, *Radiat. Phys. Chem.*, 2014, **97**, 374.
38 G. R. Strobl and M. Schneider, *J. Polym. Sci., Polym. Phys. Ed.*, 1980, **18**, 1343.
39 A. L. G. Biancolli, S. Bsoul-Haj, J. C. Doughlin, A. S. Barbosa, R. R. de Sousa Jr, O. Rodrigues Jr, A. J. C. Lafredi, D. R. Dekel and E. I. Santiago, *J. Membr. Sci.*, 2022, **641**, 119879; B.-S. Ko, K. Yoshimura, A. Hiroki and Y. Maekawa, *J. Polym. Sci.*, 2021, **59**, 108.
40 C. S. Cruz, N. Stribeck, H. G. Zachmann and F. J. B. Calleja, *Macromolecules*, 1991, **24**, 5980.

